# Advection-Enhanced Heat and Mass Transport from Neutrally Suspended Droplet in Simple Shear Flow

Yanxing Wang<sup>1,\*</sup>, David Vazquez<sup>1</sup>, Hui Wan<sup>2</sup>, Ruben Gonzalez Pizarro<sup>1</sup>, and Fangjun Shu<sup>1</sup>,

<sup>1</sup>Department of Mechanical and Aerospace Engineering, New Mexico State University, Las Cruces, NM 88003, USA

<sup>2</sup>Department of Mechanical and Aerospace Engineering, University of Colorado, Colorado Springs, CO 80918, USA

Advection-enhanced heat and mass transport from a single droplet neutrally suspended in a simple shear flow has been studied using high-fidelity numerical simulation. The capillary number ranges from 0.01 to 0.5, which encompasses the entire range of small deformation, large deformation, and breakup of the droplets. The Reynolds number is from 0.01 to 1, including regions of both weak and strong advection. The temperature and mass concentration are modeled as the concentration of a passive scalar released at the droplet surface. Two Schmidt numbers, 10 and 100, are considered, for which flow advection plays a role in the transport of passive scalar. For unbroken droplets, the interaction between the carrier fluid and the suspended droplet leads to several different flows around the droplet. The fluid motions together with scalar diffusion constitute a coupled transport mechanism for passive scalar. The dependence of scalar release rate on Reynolds and Peclet numbers can be roughly described by the correlation for a rigid sphere. For broken droplets, the basic flow features around the droplet during the process of elongation and breakup are the similar to those of an unbroken droplet. The variation of scalar release rate can be decomposed into several stages, corresponding to the process of droplet elongation and breakup. The variation of scalar release rate exhibits a high correlation with the capillary, Reynolds, and Peclet numbers. This suggests that it is feasible to develop an empirical model that incorporates the effects of the number and size distributions of child droplets after breakup.

<sup>\*</sup>yxwang@nmsu.edu

## 1. Introduction

Micro droplets ranging from tens to hundreds of microns in diameter provide an ideal platform for micro reaction, synthesis, mixing, and bioassay, due to their fast heat transfer, efficient mixing, and short residence time<sup>1,2</sup>. Flows containing finite numbers of droplets have thus been widely utilized in a diverse range of chemical and biological processes, including chemical and biochemical screening<sup>3,4</sup>, protein crystallization<sup>5,6</sup>, and enzymatic kinetic assays<sup>7,8</sup>. Larger-scale droplet systems, known as emulsions, have been applied in more fields, including energy conversion and storage<sup>9,10</sup>, liquid extraction of chemical materials<sup>11,12</sup>, synthesis of composite materials<sup>13,14</sup>, and chip sealing<sup>15,16</sup>. These applications involve complex heat and mass transport between the dispersed droplets and the continuous fluid, and have strict requirements for the transport process. A newly emerging area in which droplet mass transfer plays an important role is the development of droplet-based microscale robots, which offers great promise for diverse biomedical applications, including targeted drug delivery<sup>17,18</sup> and nanoliter-scale protein crystallization and screening<sup>19,20</sup>. Precise control of heat and mass transport is one of the key considerations in the design and development of these applications, but the current understanding of the transport mechanisms of multiphase flows is far from adequate<sup>21</sup>.

In multiphase flows, dispersed liquid droplets and gas bubbles have two major types of motion relative to the continuous fluid: the vertical movement driven by gravity or buoyancy, and the spinning caused by local flow shear. Vertical movement occurs when there is a difference in the densities of the dispersed and continuous phases, as in vapor bubbles in a boiling heat transfer system<sup>22</sup>. Considerable experimental and numerical effort has been devoted to this topic<sup>23-26</sup>. In commonly used liquid-liquid systems, however, the droplet density is comparable to that of the continuous liquid, which reduces the buoyancy effect, and the enhanced viscous effect at the microscale suppresses translational movement. Therefore, droplet spinning due to local flow shear is more important, leading to different mechanisms for heat and mass transport. Typical examples include droplet-based drug delivery in blood vessels, and heat transfer using emulsion as transfer medium. The droplets in these applications are subjected to strong flow shear<sup>26</sup>. For a droplet in a simple shear flow, the Reynolds number (Re) is defined based on the local flow shear rate and droplet radius,  $Re \equiv SR^2/v$ ,

where S is the flow shear rate, R the droplet radius, and v is the kinematic viscosity of the continuous fluid. The Prandtl (Pr) and Schmidt (Sc) numbers quantifies the ratios of momentum diffusivity to thermal and mass diffusivities, respectively. They are defined as  $Pr \equiv v/\alpha$  and  $Sc \equiv v/D_m$ , where  $\alpha$  is the thermal diffusivity and  $D_m$  is the mass diffusivity of the carrier fluid. The effect of flow shear on droplet heat and mass transfer can be characterized by Peclet number (Pe), which is defined as the ratio of advective to diffusive transfer rates,  $Pe \equiv SR^2/\alpha$  for heat and  $Pe \equiv SR^2/D_m$  for mass. Pe can also be expressed as the product of Re and Pr (or Sc). Liquid water is usually used as the main component of the continuous phase. For heat transfer, the Prandtl number of water roughly ranges from 1 to 10. For mass transfer, the Schmidt number for the diffusion of drug molecules in water can be up to  $O(10^4)^{27}$ . A simple estimation of the Peclet number of a droplet at the inner wall of a micro channel suggests that Pe may be much greater than 1, indicating that flow shear has a significant impact on the heat and mass transfer of dispersed droplets in many applications.

In the presence of flow shear, interface tension at the surface of a droplet constrains droplet shearing and generates droplet-scale recirculating flows inside and outside the droplet<sup>28-29</sup>. We found that the local flow recirculation acts as a micro mixer, which may enhance the heat and mass exchange between dispersed droplets and the continuous fluid that surrounds them. When the droplet size is large or the droplet surface tension is small, however, the droplet's surface tension cannot resist the tearing of flow shear stress, and the droplet will deform or even break up<sup>28-29</sup>. Deformation and breakup not only increase the droplet surface area, which enhances the diffusive heat and mass transfer, but also create spatial anisotropy in the material properties of the mixture. We discovered that the deformation and breakup of a droplet, in particular, impose a complex transient hydrodynamic effect on heat and mass transfer around it.

Addressing the heat and mass transport of a single droplet is the key to revealing the transport mechanism of multi-droplet systems. Over recent decades, numerous theoretical, experimental, and computational studies have been performed with the intent of understanding the behaviors of a single droplet in a shear flow<sup>28-40</sup>. The pioneering work of Taylor<sup>28,29</sup> indicates that two nondimensional parameters govern the behavior of a single droplet in a Stokes flow, the capillary number (Ca) which characterizes the relative effect of viscous force versus surface tension force, and the viscosity ratio ( $\gamma$ ) which is defined as the ratio of dynamic viscosities of

the droplet to the carrier fluid. Above a critical capillary number  $Ca_{crit}$ , which depends on  $\gamma$ , the droplet will break up. When  $Ca < Ca_{crit}$ , the droplet will evolve into a steady elliptical or elongated nonelliptical shape.  $Ca_{crit}$  reaches a minimum for  $\gamma$  between 0.1 and 1. At very high viscosity ratios, the droplet will not break up. Grace<sup>30</sup> further discovered through experiments that as  $\gamma$  goes from 1 to a critical viscosity ratio  $\gamma_{crit}$  ( $\approx$  4),  $Ca_{crit}$  increases asymptotically to infinity. For  $\gamma > \gamma_{crit}$ , droplets will tumble during the startup of flow until an elliptical droplet is obtained. In addition to the capillary number and viscosity ratio, droplet behaviors are also governed by the Reynolds number and the confinement ratio which is defined as the ratio of the separation of two parallel confining plates to droplet radius. Many studies have shown that an increase in Re can cause larger droplet deformation and decrease the  $Ca_{crit}$  at which the droplet breaks up<sup>31-34</sup>. On the other hand, a decrease in confinement ratio can enhance droplet deformation and breakup<sup>35-40</sup>. In these studies, the characteristics of the flow around the droplet were rarely touched, partially causing the gap in the knowledge of droplet heat and mass transport.

As an initial exploration of the complex transport mechanism in droplet systems, therefore, this paper focuses on the heat and mass transport from a single droplet neutrally suspended in a simple shear flow. The primary goal is to identify the complex transport mechanisms induced by the fluid dynamics due to the interaction of the suspended droplet and the carrier fluid. To this end, we take advantage of the well-developed Volume-Of-Fluid (VOF)-based code Gerris<sup>41,42</sup>, and extensively investigate the process of transport of a passive scalar from a single droplet neutrally suspended in a simple shear flow. Gerris is an open-source software developed by Stéphane Popinet<sup>41,42</sup> for incompressible multi-phase flows. The physical model is presented in Section 2. The numerical methods are described in Section 3. The grid independence study is given in Section 4. The results are analyzed in Section 5, and conclusions are presented in Section 6.

## 2. Physical Model

In order to reveal the most fundamental transport mechanism under the simplest conditions, this study is limited to the case where the droplet density and viscosity are the same as those of the carrier fluid. Figure 1 shows a schematic of the physical model. An incompressible flow with a single neutrally suspended droplet is confined by two parallel plates moving in opposite directions with speed  $U_0$ , creating a background shear rate.

The droplet is allowed to deform and break up in response to pressure and shear stress exerted by the surrounding fluid. The distance between the two plates is 2H, and the length and width of the planes are 2L and 2W, respectively. The undisturbed shear rate of the flow is defined as:

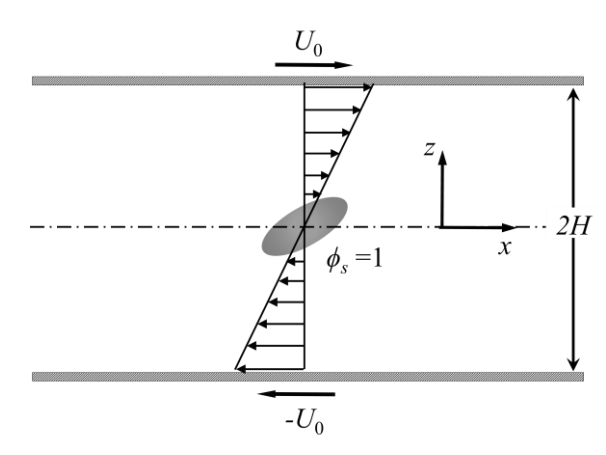


Fig. 1. Physical model of a single droplet neutrally suspended in a simple shear flow with passive scalar released from droplet surface. Zero scalar flux condition is applied on the top and bottom planes.

$$S = \frac{U_0}{H} \tag{1}$$

The behaviors of the droplet are primarily determined by capillary number (Ca) and viscosity ratio ( $\gamma$ ). In this study, the density and viscosity of the droplet are the same as the carrier fluid. The capillary number is defined as,

$$Ca \equiv \frac{\mu RS}{\sigma} \tag{2}$$

where  $\mu$  is the dynamic viscosity of the droplet and the carrier fluid,  $\sigma$  the interfacial tension, and R the spherical radius of the droplet without deformation. The droplet behaviors are also influenced by Reynolds number, which is defined based on the droplet radius R and the background flow shear rate S,

$$Re \equiv \frac{SR^2}{\nu} \tag{3}$$

where  $\nu$  is the kinematic viscosity of the droplet and the carrier fluid.

To predict heat and mass transport, temperature and mass concentration are modeled as the concentration  $(\phi)$  of a passive scalar released at the droplet surface, where  $\phi$  is fixed at  $\phi_s=1$ . The Peclet number, which characterizes the effect of flow shear on scalar transport, is defined as

$$Pe \equiv \frac{SR^2}{D_{rm}} = ReSc \tag{4}$$

where  $D_m$  is the diffusivity of the passive scalar in the carrier fluid, and Sc is the Schmidt number which is defined as.

$$Sc \equiv \nu/D_m$$
 (5)

The Reynolds number is a parameter related to the motion of fluid and can be modified by changing the characteristic fluid velocity and length scale, while the Schmidt number is a parameter of the material properties of the fluid. The transport of passive scalar is primarily determined by Peclet number which is the product of Re and Sc.

To compare the scalar release rate of the deformed droplets, it is convenient to use the nondimensional release rate, i.e. the Sherwood number (Sh), which is defined based on the radius and surface area of the spherical radius of the droplet without deformation,

$$Sh \equiv \frac{QR}{D_m A \phi_S} \tag{6}$$

where Q is the release rate of the passive scalar from the particle surface,  $A (= 4\pi R^2)$  the surface area of the sphere, and  $\phi_s$  (= 1) the concentration of passive scalar at the droplet surface.

A complete description of the problem includes the capillary number (Ca), Reynolds number (Re), Schmidt number (Sc) or Peclet number (Pe), and the ratios of the height (2H), width (2W), and length (2L) of the computational domain to the radius of the droplet (2H/R, 2W/R, and 2L/R).

# 3. Numerical Methods

A well-developed VOF-based CFD solver is applied in conjunction with an efficient adaptive mesh refinement (AMR) technique to simulate the droplet-scale fluid dynamics and scalar transfer. The conservation equations of mass, momentum, and temperature or scalar concentration take the following form,

$$\frac{\partial \rho}{\partial t} + \nabla \cdot (\rho \mathbf{u}) = 0 \tag{7}$$

$$\frac{\partial(\rho \mathbf{u})}{\partial t} + \nabla \cdot (\rho \mathbf{u} \otimes \mathbf{u}) = -\nabla p + \nabla \cdot (2\mu \mathbf{E}) + \sigma \kappa \delta_s \mathbf{n}$$
(8)

$$\frac{\partial(\rho\phi)}{\partial t} + \nabla \cdot (\rho\phi\mathbf{u}) = \nabla \cdot (\rho D\nabla\phi) \tag{9}$$

where  $\bf u$  is the velocity vector,  $\rho$  the density of the droplet and carrier fluid, p the pressure,  $\bf E$  the strain rate tensor, and  $\bf n$  the unit normal vector pointing outward from the droplet surface. In the momentum equation, the surface tension is treated as a continuous body force as  $\sigma\kappa\delta_s{\bf n}$ , where  $\sigma$  is the surface tension of the droplet in the carrier liquid,  $\kappa$  the interface curvature, and  $\delta_s$  the Dirac-delta function. The VOF approach is used to capture the time-evolving interface between the droplet and the carrier liquid. The transport equation for volume fraction reads

$$\frac{\partial F}{\partial t} + \mathbf{u} \cdot \nabla F = 0 \tag{10}$$

where F is the volume fraction of droplet phase in the grid cells. F = 1 in the droplet phase and F = 0 in the carrier fluid phase. The density and dynamic viscosity thus are written as,

$$\rho = F\rho_d + (1 - F)\rho_c$$
 and  $\mu = F\mu_d + (1 - F)\mu_c$  (11)

In this study, a simple case is considered, in which the fluid is incompressible in both the droplet and the carrier fluid, and the density and viscosity are constant,

$$\rho_d = \rho_c = \text{constant} \quad \text{and} \quad \mu_d = \mu_c = \text{constant}$$
(12)

Equations (7)-(12) constitute the system of governing equations for two-phase flows with scalar transfer in an incompressible fluid.

A time-staggered projection method is used to solve the equations,

$$\rho \mathbf{u}^* - \Delta t \nabla \cdot (\mu \mathbf{E}^*) = \Delta t \nabla \cdot (\mu \mathbf{E}^n) + \Delta t (\sigma \kappa \delta_s \mathbf{n})^{n+1/2} + \rho \mathbf{u}^n - \Delta t \rho \mathbf{u}^{n+1/2} \cdot \nabla \mathbf{u}^{n+1/2}$$
(13)

$$\nabla \cdot \left(\frac{\Delta t}{\rho} \nabla p^{n+1/2}\right) = \nabla \cdot \mathbf{u}^* \tag{14}$$

$$\mathbf{u}^{n+1} = \mathbf{u}^* - \frac{\Delta t}{\rho} \nabla p^{n+1/2} \tag{15}$$

The transport equation for scalar concentration is discretized by an explicit scheme at each time level,

$$\phi^{n+1/2} = \phi^{n-1/2} - \Delta t \nabla \cdot (\phi^n \mathbf{u}^n) + \Delta t \phi^n \nabla \cdot \mathbf{u}^n + \Delta t \nabla \cdot (D \nabla T^n)$$
(16)

The transport equation for volume of fluid is also discretized by an explicit scheme,

$$F^{n+1/2} = F^{n-1/2} - \Delta t \mathbf{u}^n \cdot \nabla F^n \tag{17}$$

The spatial discretization of Eqns. (13)-(17) is realized through a graded quadtree partitioning. The details are given in Popinet<sup>41-42</sup>. An AMR technique with multiple-level resolution developed by Popinet<sup>41,42</sup> is used to resolve the flow and scalar fields. During the simulation, the grid resolution is dynamically adjusted according to the deformation of the droplet and the concentration of passive scalar. The grid resolution is highest near the droplet and gradually decreases toward the far field. Several refinement criteria are used concurrently, depending on the physical conditions encountered, to ensure numerical accuracy and robustness. These include gradient-based, value-based, and curvature-based refinements. The gradient-based criterion ensures adequate grid refinement in the regions with steep change in the variables of interest, and avoids unnecessary refinement in regions with smooth change. The value-based criterion ensures the accurate prediction of scalar transport in the regions with higher scalar concentration. The curvature-based criterion enables the precise capture of large curvature deformation in a small area.

# 4. Grid Independence Study

To examine the grid sensitivity of the results, we conducted simulations of fluid flow and scalar transport around a droplet for Ca=0.3, Re=1 and Sc=100. Three different sets of grids, with  $N_p=25$ , 50, and 100, are used around the droplet, where  $N_p$  is the number of grid points over one diameter of an undeformed droplet. Figure 2 shows the three grid systems around the droplet. In Fig. 3 we compare the distributions of streamwise velocity,  $u_x$ , and the concentration of passive scalar,  $\phi$ , along the vertical line through the droplet center, among the three grid systems. As shown in the figure, the profiles of  $u_x$  are in good agreement with each other. However, as  $N_p$  increases from 25 to 50, the profile of  $\phi$  changes obviously near the droplet surface, indicating a deviation in the flux of passive scalar released at droplet surface. The larger  $N_p$  produces a more accurate result. When  $N_p$  increases from 50 to 100, the maximum relative deviation near the droplet surface decreases

to less than 1%. Considering the result accuracy and the computing time requirements, the grid of  $N_p = 50$  is used in the extensive simulations.

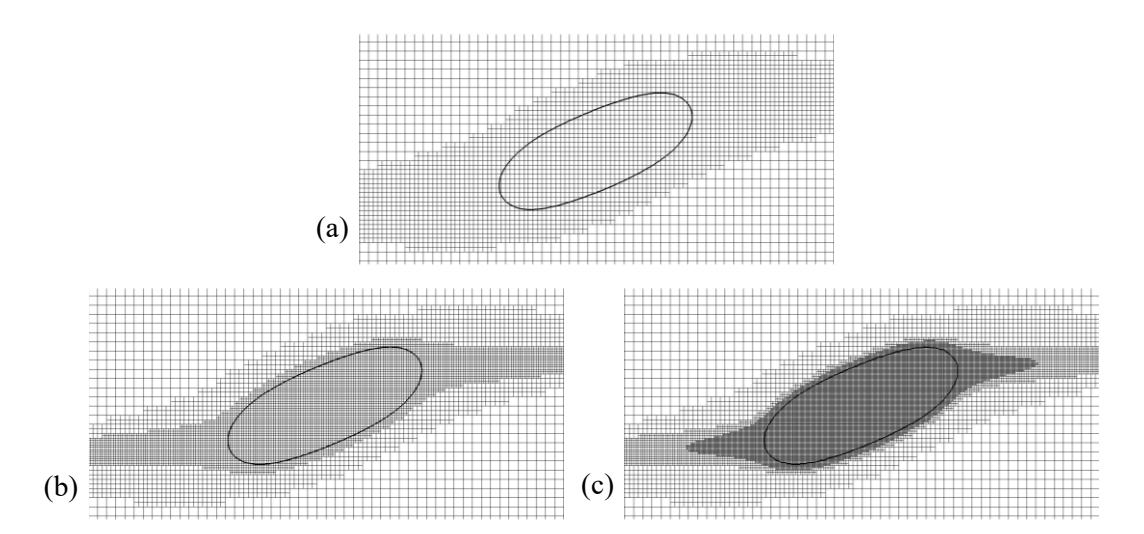


Fig. 2. Grid resolutions around a droplet, for Re = 1 and Sc = 100. Finer grids are used around the droplets according to the gradient-, value-, and curvature-based criteria. (a)  $N_p = 25$ , (b)  $N_p = 50$ , and (c)  $N_p = 100$ , where  $N_p$  is the number of grid points over one diameter of an undeformed droplet.

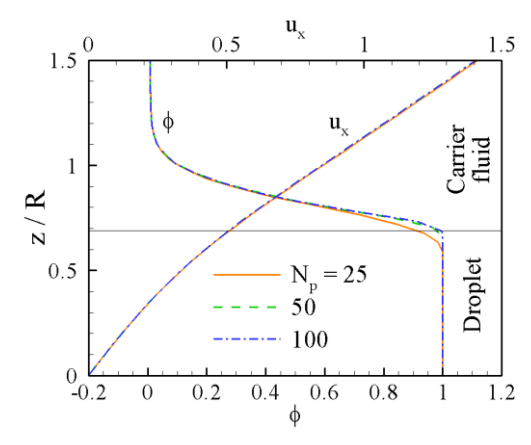


Fig. 3. Effect of grid resolution on streamwise velocity  $(u_x)$  and concentration of passive scalar  $(\phi)$  along the vertical line through the droplet center, for Ca = 0.3, Re = 1 and Sc = 100. The horizontal line roughly indicates the droplet surface.

## 5. Results and Discussion

# 5.1 Unbroken droplets

In this section, the fluid dynamics and scalar transport in a system of a single droplet are analyzed. Emphasis is placed on the flow characteristics induced by the interaction between the suspended droplet and the carrier fluid, and the mechanism of scalar transport from the droplet to the ambient fluid influenced by fluid dynamics. The capillary number considered in this study ranges from 0.01 to 0.5, which encompasses the entire range of small deformation, large deformation, and breakup of the droplet. The Reynolds number is from 0.01 to 1, which includes the regions of weak and strong advection. Two Schmidt numbers, Sc = 10 and 100 are considered, for which flow advection plays a role in the transport of passive scalar. As shown in Sibillo et al.<sup>36</sup>, the influence of flow boundaries on droplet deformation is negligible when 2H/R > 10. This study focuses on the mechanisms under conditions with little or no boundary effect. The ratios of the length (x direction), width (x direction), and height (x direction) of the computational domain to the radius of the undeformed droplet are fixed at x and x and x and x and x and x are the droplet does not break up, the flow evolution and scalar transfer eventually reach a steady state, in which the droplet shape, flow velocity at each point, and rate of scalar transfer from the droplet no longer change with time. The analysis is carried out in the steady state. In the cases with droplet breakup, the analysis is carried out throughout the whole process.

First, we use the case of Ca = 0.1 to demonstrate the basic flow structure and scalar transport around a droplet with a small deformation. At lower Reynolds numbers, the viscous effect is stronger and the streamline topology is more pronounced. Figure 4 shows the typical streamlines around a droplet at Re = 0.1. In the steady state, the streamlines coincide with the trajectories of the fluid particles, so the streamlines depict the transport of passive scalar via flow advection. As shown in the figure, the flow is composed of several different streamline patterns. On the lateral sides, some fluid originating upstream of the droplet is entrapped into a recirculation zone, in which the fluid spirals toward the droplet in a cone-shaped pattern. At the droplet surface the fluid splits into two parts. One part spirals inward (decreasing radial coordinate; red lines) along the droplet surface toward the axis of rotation, then leaves the droplet around the axis. The other part spirals outward (increasing radial coordinate; blue lines) along the droplet surface toward the central x-z plane, then leaves the droplet on the central x-z plane. Outside the spiral flows, the fluid passes the droplet and travels downstream directly (orange lines), wrapping around the spiral flows. The patterns of the spiral flows are similar to those around a rigid sphere or an oblate spheroid  $^{43,44}$ , but the spiral is outward on the sides and inward near the

equator around a rigid particle. It has been shown by Singh and Sarkar<sup>45</sup> that the spirals around a droplet can be either the same as those shown in Fig. 4 or the same as those of a solid sphere, depending on the viscosity ratio. A rigid sphere can be seen as an extreme case of droplet with an infinite viscosity ratio. When the viscosity ratio is much larger than 1, the flow directions around a droplet are the same as those around a rigid sphere.

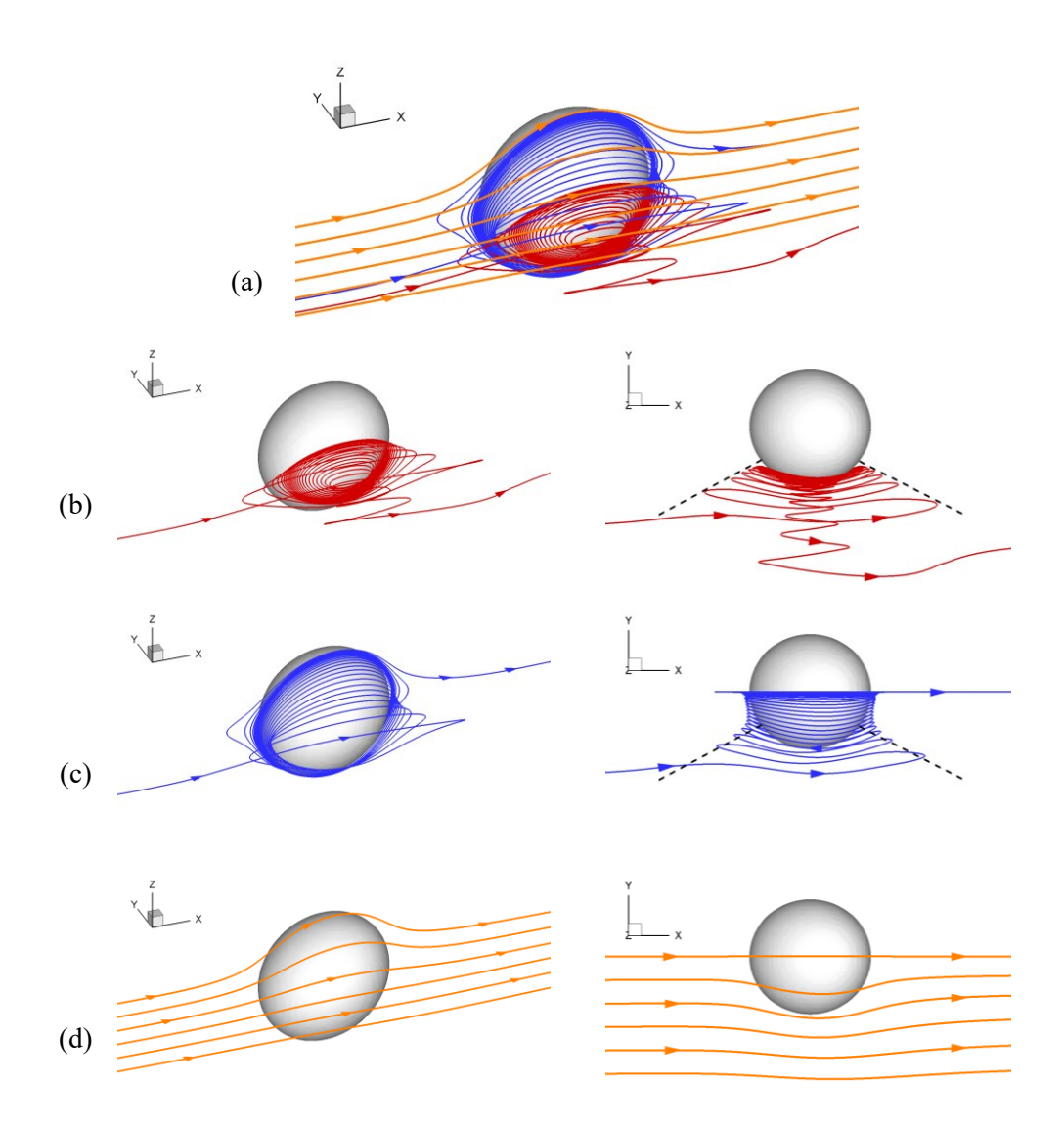


Fig. 4. Typical 3D streamlines around a droplet for Ca = 0.1 and Re = 0.01. (a) Overall pattern of streamlines around the droplet, (b) inward (decreasing radial coordinate) spiral flow on the sides. This flow originates upstream of the droplet at some distance from the central x-z plane and leaves the droplet near the axis of rotation, (c) outward (increasing radial coordinate) spiral flow on the sides. This flow originates upstream of the droplet at some distance from the central x-z plane and leaves the droplet near the central x-z plane, (d) outer passing flow enwrapping the spiral flows.

As the Reynolds number increases, the area of influence of the droplet, which depends on the viscosity of the fluid, decreases on the lateral sides. Figure 5 shows the streamlines around a droplet for Ca = 0.1 and Re = 1. Compared with the streamlines for Re = 0.1 shown in Fig. 4, the lateral extension of the spiral flows in the cone pattern and around the axis of rotation is significantly reduced. In addition, the increased fluid inertia creates a recirculating wake on either side of the oblate spheroid along the flow axis; the fluid approaches the droplet near the axis and then turns back before touching the spheroid (purple lines). The recirculating wakes are separated from the spiral flows surrounding the droplet by two lines of saddle points. The spiral flows and the recirculating wakes are enwrapped by the outer passing flow, which drives the recirculating flow inside and outside the droplet, as well as the motion of the recirculating wake. The behaviors of these flow components and the interactions among them work as an ensemble to form a complex mechanism for the transport of passive scalar.

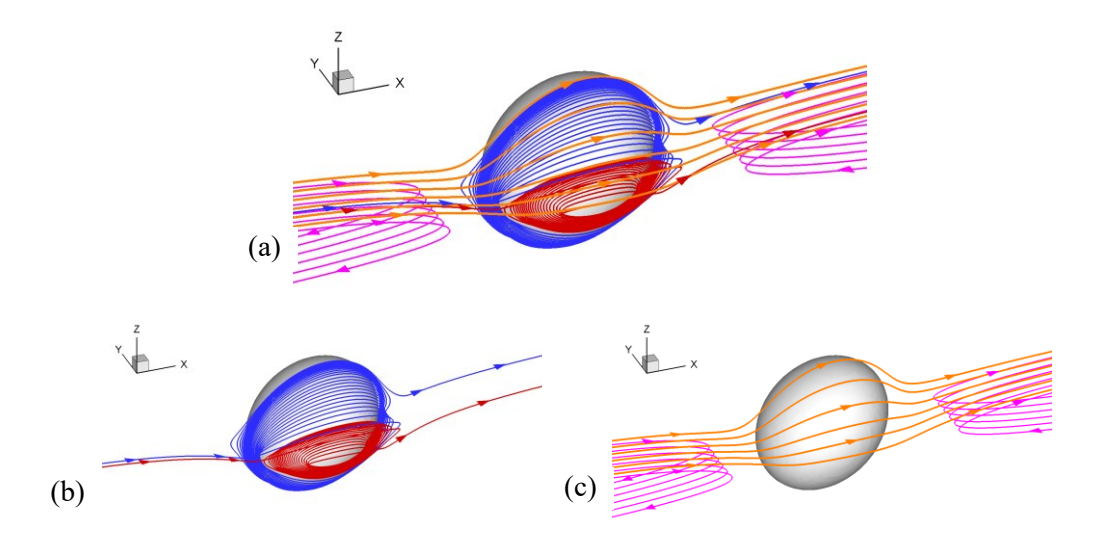


Fig. 5. Typical 3D streamlines around a droplet for Ca = 0.1 and Re = 1. (a) Overall pattern of streamlines around the droplet, (b) inward (decreasing radial coordinate) and outward (increasing radial coordinate) spiral flows on the sides, (c) outer passing flow and recirculating wake flow.

Under the action of the surrounding flows, scalar transport exhibits a different pattern from that of diffusion transport. Figure 6 shows the scalar concentration ( $\phi$ ) together with the 3D streamlines around a droplet for Ca = 0.1, Re = 1 and Sc = 100. The capillary and Reynolds numbers are the same as in Fig. 5. On the windward sides (upper left and lower right) of the droplet, the impact of the outer flow significantly decreases the thickness of scalar boundary layer, through which  $\phi$  decreases from 1 at the droplet surface to 0 in the

ambient fluid. On the leeward sides (upper right and lower left), the passive scalar released at the droplet surface is carried by the passing flow and advected downstream. On the lateral sides, the passive scalar is transported laterally from the droplet surface to the ambient fluid through a scalar boundary layer that is thicker than that on the windward sides. Compared with pure diffusion, the pattern shown in this figure is the outcome of a more complex transport mechanism. It is seen in Fig. 5 that the droplet is surrounded by a flow layer consisting of an inward and an outward spiral flow on the lateral sides. The passive scalar released at the spheroid surface, therefore, is first transferred to the surrounding spiral flows via pure diffusion. In the extreme case of  $Sc = \infty$ , where the molecular diffusivity  $D_m = 0$ , the released passive scalar will be transported away from the droplet surface by the surrounding spiral flows via pure advection. The spiral streamlines depict the path of scalar transport. In the case of finite Schmidt number (Sc), molecular diffusion provides important scalar transport across the streamlines. As shown in Figs. 6(c) and (d), the outer passing flow hits the windward sides (upper left and lower right sides) of the droplet and then travels downstream along the top and bottom surfaces as well as the lateral sides of the droplet. During this process, the passing flow gains passive scalar from the spiral flows surrounding the droplet via molecular diffusion across the streamlines. As a result, the scalar concentration  $(\phi)$  of the passing flow increases gradually. Since the spiral flows exist only in the thin layer on the droplet surface, the spiral flows lose most of their passive scalar to the passing flow when they

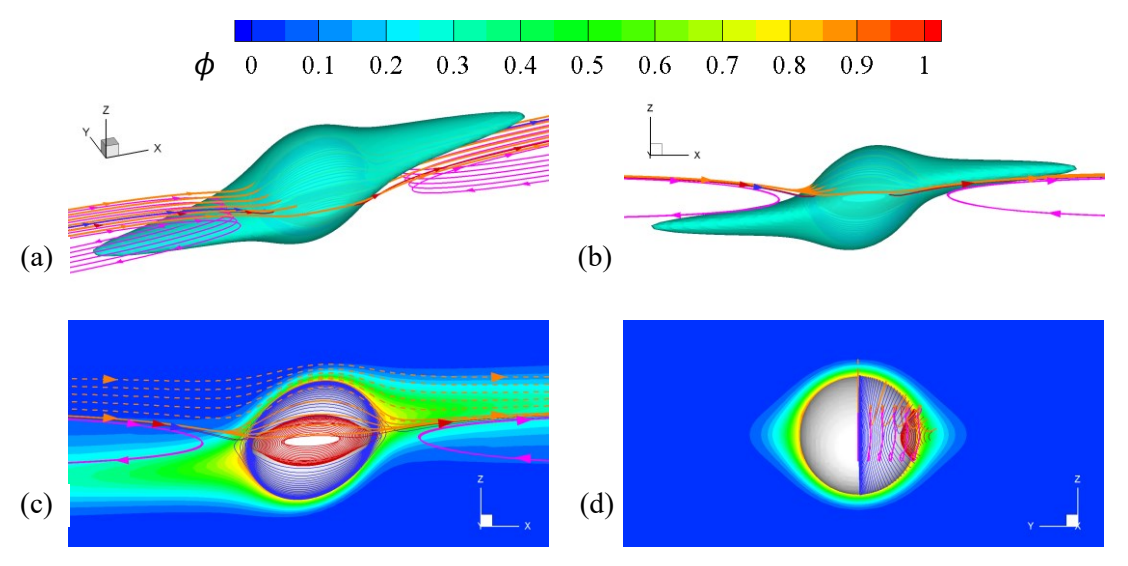


Fig. 6. Patterns of scalar concentration,  $\phi$ , around a droplet for Ca = 0.1, Re = 1 and Sc = 100. (a, b) 3D iso-surfaces of  $\phi = 0.3$  with the typical streamlines, (c, d) iso-contours of  $\phi$  on the central x-z and y-z planes.

leave the droplet, and the outer passing fluid transports most of the passive scalar downstream via flow advection.

To accentuate the diffusion process, we plot the normalized modulus of the gradient of scalar concentration  $(R||\nabla\phi||)$  along with the 3D streamlines around the droplet in Figs. 7. It can be seen that the diffusion transport occurs primarily in four regions. The first is in the flow layer on the windward droplet surface, where passive scalar is transported from the droplet surface to the spiral flows, then to the outer passing flow. The second is downstream of the leeward side, where passive scalar is transported from the outer flow just past the droplet surface to the flow further outside. The third is in the wake flow near the flow axis (z=0), where the passive scalar is transported from the passing flow to the downstream part of the spiral flows, and then to the recirculating wake flow near the axis. The recirculating wake flows also help transport passive scalar downstream. The fourth region is the layer of spiral flows on the lateral sides of the droplet, where the passive scalar is transported from the droplet surface to the spiral flows, and then to the outer passing fluid. During this process, the spiral flows on droplet surface, the recirculating wake flows on the axis, and the outer passing flow together form a coupled transport mechanism for the passive scalar, involving both molecular diffusion and flow advection.

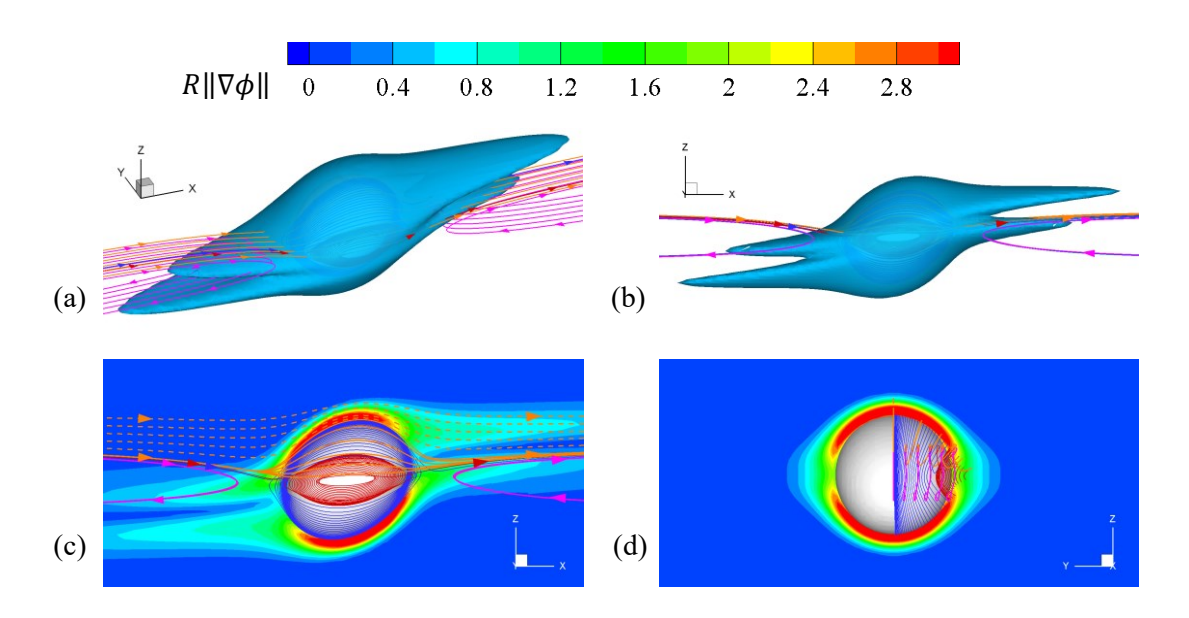


Fig. 7. Mechanism of transport of passive scalar illustrated by the patterns of the magnitude of the gradient of scalar concentration,  $R\|\nabla\phi\|$ . (a, b) 3D iso-surfaces of  $R\|\nabla\phi\|$  at 0.5, (c, d) iso-contours of  $R\|\nabla\phi\|$  on the central x-z and y-z planes.

The increase in capillary number leads to larger droplet deformation. The droplet is elongated and aligns itself toward the flow direction. When  $Ca < Ca_{crit}$ , the droplet gradually approaches a stable elliptical or elongated shape, and the fluid flow and scalar transport evolve toward a steady state. The deformation not only increases the droplet surface area, but also alters the flow pattern around the droplet. Figure 8 shows the typical streamlines around a droplet for Ca = 0.3 and Re = 1. Although the droplet is greatly elongated, the streamline pattern is maintained, and looks similar to the case for Ca = 0.1 shown in Fig. 5. The droplet is surrounded by inward and outward spiral flows on each side. Along the flow axis, there is a recirculating wake before and after the droplet. The spiral flows and wake flows are enwrapped by the outer passing flow. The spiral flows do not extend very far in the lateral direction, due to the larger Reynolds number.

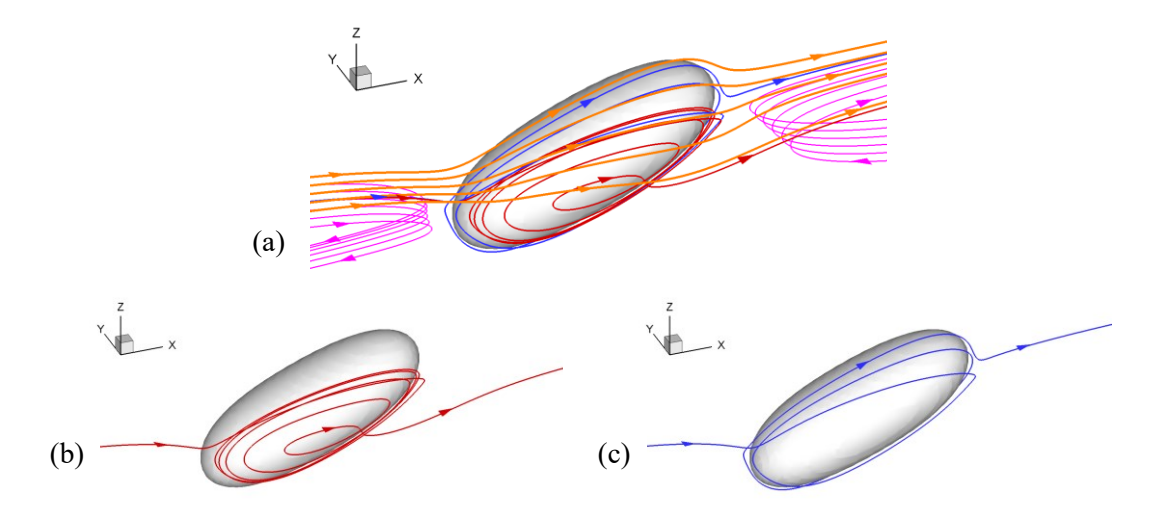


Fig. 8. Typical 3D streamlines around a droplet for Ca = 0.3 and Re = 1. (a) Overall pattern of streamlines around the droplet, (b) inward (decreasing radial coordinate), (c) outward (increasing radial coordinate) spiral flows on the sides.

Figure 9 shows the scalar concentration ( $\phi$ ) together with the streamlines around a droplet for Ca=0.3, Re=1, and Sc=100. The basic pattern of  $\phi$  and the streamlines is similar to that of Ca=0.1, as shown in Fig. 6. As a result, the deformation of the droplet does not change the mechanism of scalar transport around it. An important question to address, however, is whether the deformation of the droplet significantly alters the transport efficiency. Table 1 gives the droplet aspect ratio  $\Lambda$  ( $\equiv L_{max}/L_{min}$ , where  $L_{max}$  and  $L_{min}$  are the longest and shortest axes, respectively) and nondimensional scalar release rate Sh at several typical Re and Ca. For Re=0.01, when Ca increases from 0.1 to 0.4,  $\Lambda$  increases from 1.25 to 2.70. The aspect ratio is more

than doubled, yet Sh only increases from 1.05 to 1.07 for Sc = 10, and from 1.33 to 141 for Sc = 100. The change is similar for Re = 1. That is, the scalar release rate does not increase as much as the aspect ratio. The main reason is that the increased elongation of the droplet and its increased inclination in the flow direction reduce the effective impact area of the ambient fluid on the droplet surface.

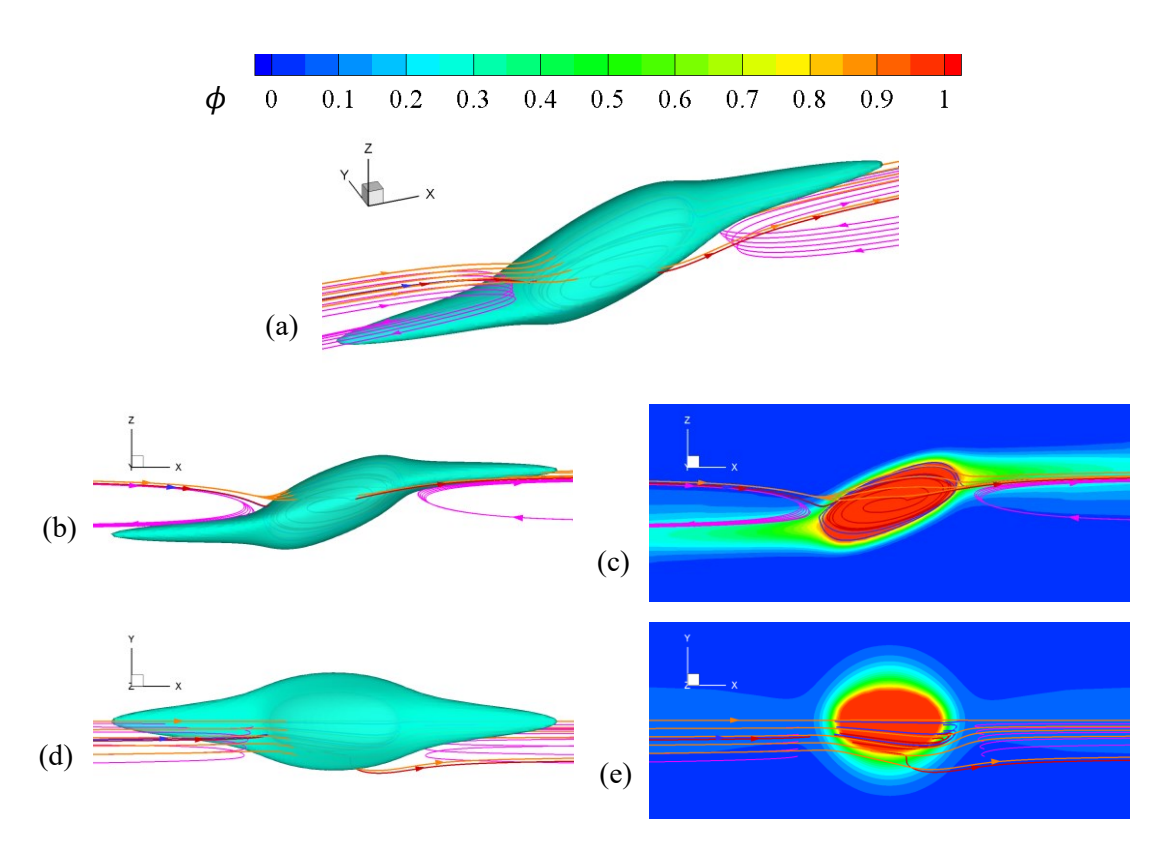


Fig. 9. Patterns of scalar concentration,  $\phi$ , around a droplet for Ca = 0.3, Re = 1 and Sc = 100. (a, b, d) 3D iso-surfaces of  $\phi = 0.3$  with typical streamlines, (c, e) iso-contours of  $\phi$  on the central x-z and y-z planes.

Table 1. Droplet aspect ratio and nondimensional scalar release rate for  $C\alpha = 0.1$  and 0.3.

Re	Са	Λ	Sh(Sc = 10)	$Sh\left(Sc=100\right)$
0.01	0.1	1.25	1.05	1.33
	0.4	2.70	1.07	1.41
1	0.1	1.27	1.94	4.03
	0.3	2.73	2.11	4.49

Since Taylor's pioneering work<sup>28,29</sup>, the deformation of a droplet is usually quantified by the Taylor deformation parameter, D, which is defined as,

$$D = \frac{L_{max} - L_{min}}{L_{max} + L_{min}} \tag{18}$$

where  $L_{max}$  and  $L_{min}$  are the longest and shortest axes of the deformed droplet, respectively. For a spherical droplet D=0, and for a droplet with large deformation, D is close but still less than one. Over the past few decades, a lot of theoretical  $^{29,35,46}$ , experimental  $^{36,38,47,50}$ , and numerical  $^{34,39,40,51}$  work has been done to identify the dependence of D on the controlling parameters, such as capillary number Ca, viscosity ratio  $\gamma$ , and confinement ratio 2H/R. Based on these results, a number of theoretical and empirical models have been developed  $^{29,35,46,47}$ . Figure 10 shows the Taylor deformation parameter of unbroken droplets versus capillary number in the stable state. The present numerical results agree well with the predictions of the theoretical models and other numerical simulations, and deviation occurs only when both Re and Ca are larger. This is because the theoretical models  $^{29,35,46,47}$  and the numerical results of Grounley et al.  $^{51}$  only deal with the case of Stokes flow and do not involve the effect of fluid inertia. As shown in the figure, for smaller Reynolds numbers, D is roughly a linear function of Ca and D=0 when Ca=0, so D/Ca is roughly constant for smaller Re.

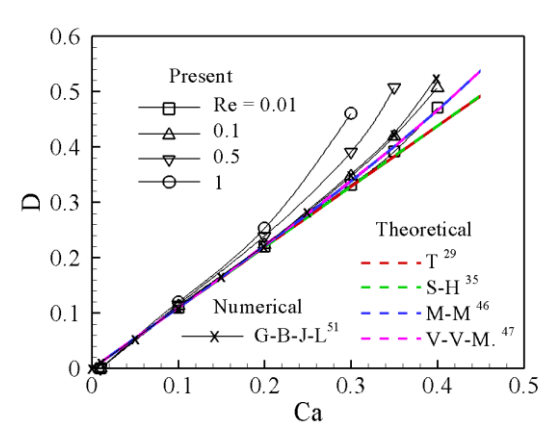


Fig. 10. Taylor deformation parameter of unbroken droplets versus capillary numbers in the stable state. Symbols represent numerical simulation data. T<sup>29</sup>: Taylor<sup>29</sup>, S-H<sup>35</sup>: Shapira and Haber<sup>35</sup>, M-M<sup>46</sup>: Maffettone and Minale<sup>46</sup>, V-V-M<sup>47</sup>: Vananroye et al. <sup>47</sup>, G-B-J-L<sup>51</sup>: Gounley et al. <sup>51</sup>.

In Fig. 11 we show the Taylor deformation parameter D and the ratio of Taylor deformation parameter to capillary number D/Ca versus Reynolds number Re. As shown in Fig. 11(a), for each Ca, D increases with increase in Re, and D is more sensitive to Re at larger Ca and Re. From Fig. 11(b) it can be seen that D/Ca is

roughly equal to 1.1 when  $Re \approx 0.01$ . As Re increases, D/Ca increases accordingly, and the increase is greater for larger Ca. This is consistent with the results of Singh and Sarkar<sup>45</sup>.

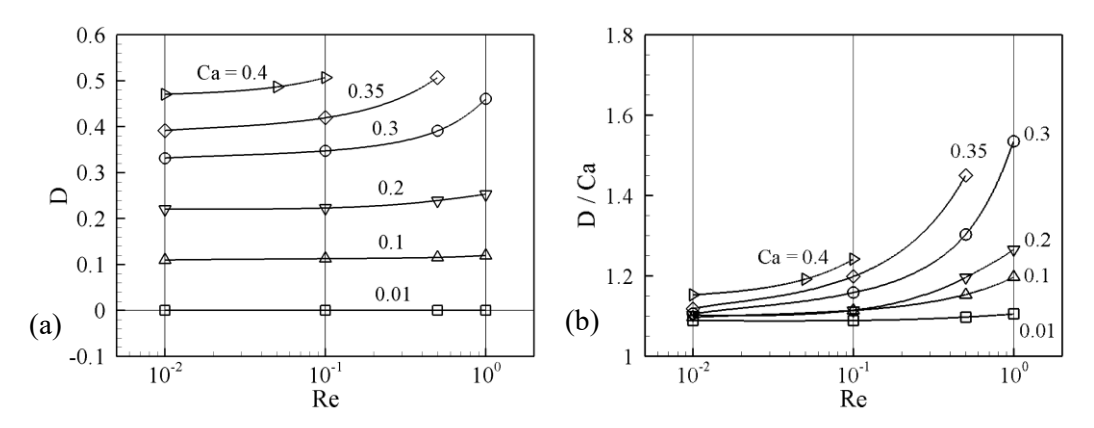


Fig. 11. Taylor deformation parameter D and the ratio of deformation parameter to capillary number D/Ca versus Reynolds number Re. (a) D vs. Re, (b) D/Ca vs. Re.

Figure 12 shows the nondimensional scalar release rate, Sherwood number Sh, versus capillary and Reynolds numbers for unbroken droplets for Sc = 100. It has been shown in Fig. 10 and 11 that droplet deformation is primarily determined by Ca, yet Ca does not cause significant change in Sh for the same Re. The increase in Ca only causes a slight increase in Sh, as shown in Fig 12(a); possible reasons have been discussed above. The variation of Sh, on the other hand, exhibits a stronger dependence on Re. The curves of Sh versus Re are close to each other, and the values of Sh increases as Re increases, following the same trend. This observation enables the development of a simple empirical model of Sh as a function of Re and Sc. When the effect of Ca is ignored, that is, when the effect of droplet deformation on scalar release rate is ignored, the

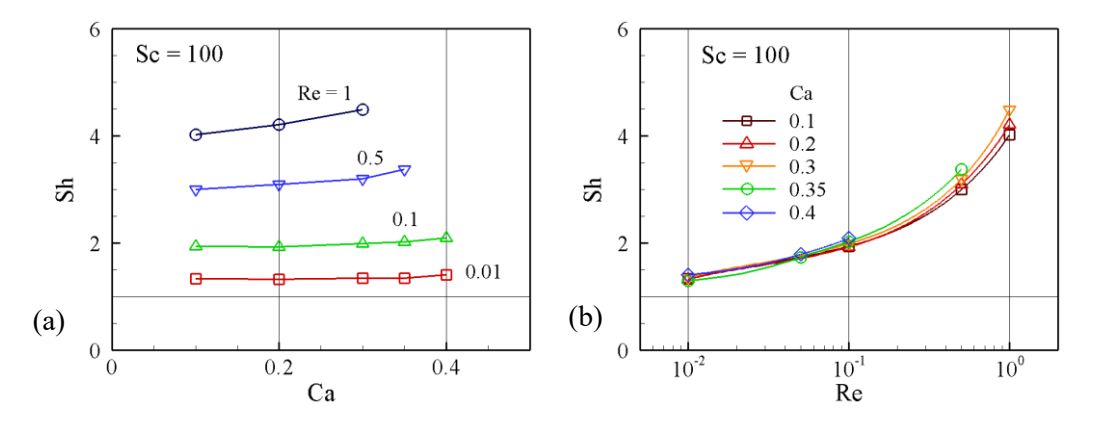


Fig. 12. Sherwood number versus capillary and Reynolds numbers for unbroken droplets. Sc = 100. Symbols represent numerical simulation data. (a) Sh vs. Ca, (b) Sh vs. Re.

model is expected to have a form similar to those of rigid spheres. Several models have been developed for rigid spheres<sup>43,52-55</sup>.

Figure 13 shows the variation of Sh with Peclet number Pe for Sc = 10 and 100, compared with the prediction of the Wang and Brasseur's model<sup>43</sup> for a rigid sphere for Re = 0. The numerical results for deformed droplets agree well with the prediction of the model up to Pe = 10. Apparent deviation can be observed when Pe > 10. When comparing the data with the model for the same Re, the deviation remains. For brevity, we do not show the comparison here. This deviation is most likely caused by the different effects of fluid inertia on a droplet as opposed to a solid sphere. In applications where accuracy is not critical, the models for rigid spheres can be used to predict the rate of scalar release from unbroken droplets.

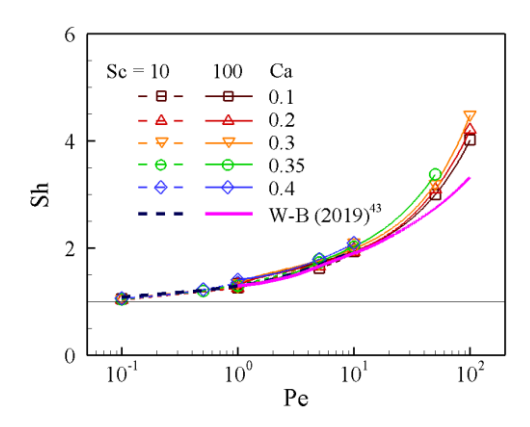


Fig. 13. Sherwood number versus Peclet number for unbroken droplets. W-B: Wang and Brasseur<sup>43</sup>.

# 5.2 Broken droplets

The increase of capillary and Reynolds numbers enhances the deformation of a droplet. When they exceed a certain range, the droplet will break up. At a given Re, the number of child droplets produced by droplet breakup increases with increased Ca; and at a given Ca, the number of child droplets increases with increased Re. Figure 14 shows the process of a single droplet breaking up into two larger droplets of roughly the same size and a third tiny droplet, as well as the process of scalar transport from the droplets, for Ca = 0.5, Re = 0.01, and Sc = 100. This is the simplest mode of droplet breakup. The patterns are plotted at several typical times in the variation of nondimensional scalar release rate, Sh, with time  $t/\tau_s$ , where  $\tau_s \equiv 1/S$  is the characteristic time based on flow shear S. Figure 15 shows the variation of Sh versus  $t/\tau_s$  for Ca = 0.3, Re = 0.3

1, and Sc = 100. The variation of Sh can be decomposed into four stages. Stage I is from  $t/\tau_s \approx 5$  to 55, in which Sh increases roughly linearly with  $t/\tau_s$ . From the patterns of droplet deformation and scalar concentration at  $t/\tau_s = 5$  and  $\approx 55$  shown in Fig. 14, it can be seen that the droplet is significantly elongated in the flow direction during this period. Therefore, it is the increase in droplet surface area due to elongation that causes the increase of Sh. It has been shown in Table 1 and Fig. 12 that for unbroken droplets, the droplet elongation does not lead to a significant increase in Sh. Yet for broken droplets, the elongation is much larger, which causes an obvious increase in Sh. Stage II is from  $t/\tau_s \approx 55$  to  $\approx 75$ , in which Sh largely remains constant. As shown in Fig. 14, the parent droplet breaks up into two larger and a tiny child droplet in this period. The extension of the droplets in flow direction does not increase very much. When  $t/\tau_s \approx 75$ , although the two larger droplets have separated completely, they are still close. The total scalar release rate is close to that before separation. (For the present purposes, we neglect the third tiny droplet.) The two child droplets lie in each other's area of higher scalar concentration, so they reduce each other's scalar release rate. In Stage III, from  $t/\tau_s \approx 75$  to  $\approx 100$ , the two droplets move away from each other and the distance between them increases with time, as shown in Fig. 14. The influence of the two child droplets on each other's scalar release gradually diminishes. Therefore, Sh increases with time in Stage III, as shown in Fig. 15. When the distance between the two child droplets is far enough that the mutual influence can be ignored, the variation of Sh enters Stage IV, which covers the entire regime of  $t/\tau_s \gtrsim 100$ . In Stage IV, the two child droplets are independent

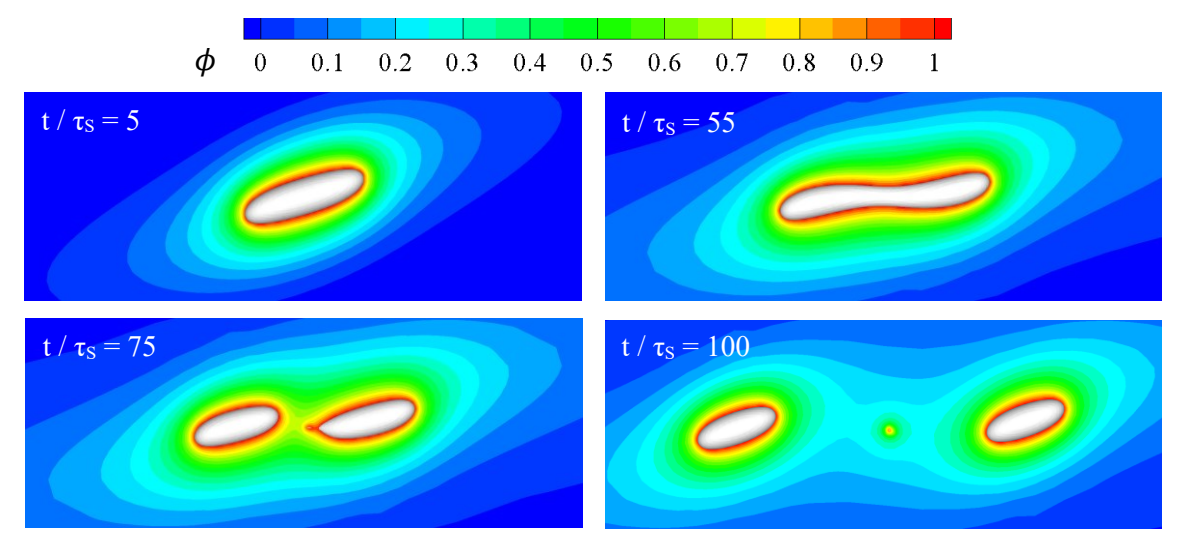


Fig. 14. Patterns of 3D droplet breakup for Ca = 0.5 and Re = 0.01 and scalar concentration on the central x-z plane for Sc = 100.

of each other and they are both in a steady state. The total scalar release rate is the sum of those of the two droplets, which remains constant over time.

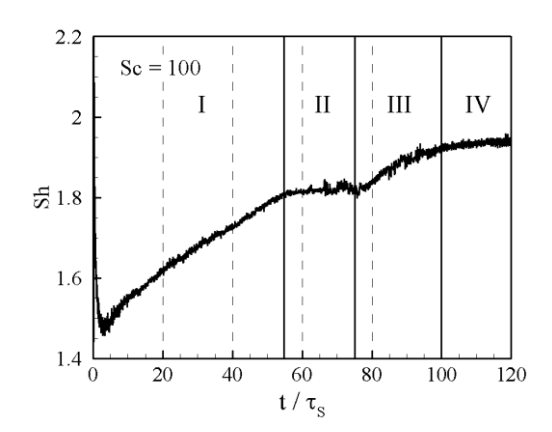


Fig. 15. Nondimensional scalar release rate from parent droplet and child droplets: Sherwood number Sh versus time  $t/\tau_s$  for Ca=0.5 and Re=0.01.

In this problem, the characteristic flow time, defined as  $\tau_s \equiv 1/S$ , is roughly the time it takes for the fluid to travel over one droplet radius. The process of droplet breakup shown in Fig. 14 suggests that the time scale of the droplet breakup is on the order of  $10^2\tau_s$ , which is much larger than the flow time. The flow characteristics around the droplets evolve slowly from the case of a single droplet (Figs. 5 and 8) to the case of two separate droplets. At each instant, the flow field can be seen to be quasi-static. The instantaneous streamlines therefore still describe to some extent the advective transport paths around the droplet. Here we are more interested in the streamline structure of the intermediate state through which a single droplet breaks up into two droplets.

Figure 16 shows the streamlines around the droplet after it has elongated into two ellipsoidal structures that have not yet separated. On the side of each ellipsoid there is an inward (decreasing radial coordinate) spiral flow, similar to that around a single ellipsoid droplet (Figs. 5 and 8). This spiral is entrapped into the recirculating flow somewhere upstream of the droplet off-central *x-z* plane and leaves the droplet around the axis of rotation of one of the two ellipsoids, as shown in Fig. 16(b) and (c). There is also an outward (increasing radial coordinate) spiral flow, which originates somewhere upstream of the droplet and recirculates around the whole system of two droplets, before leaving the droplet on the central *x-z* plane. This streamline pattern reveals the advective transport pattern of passive scalar from the droplet during the process of droplet breakup.

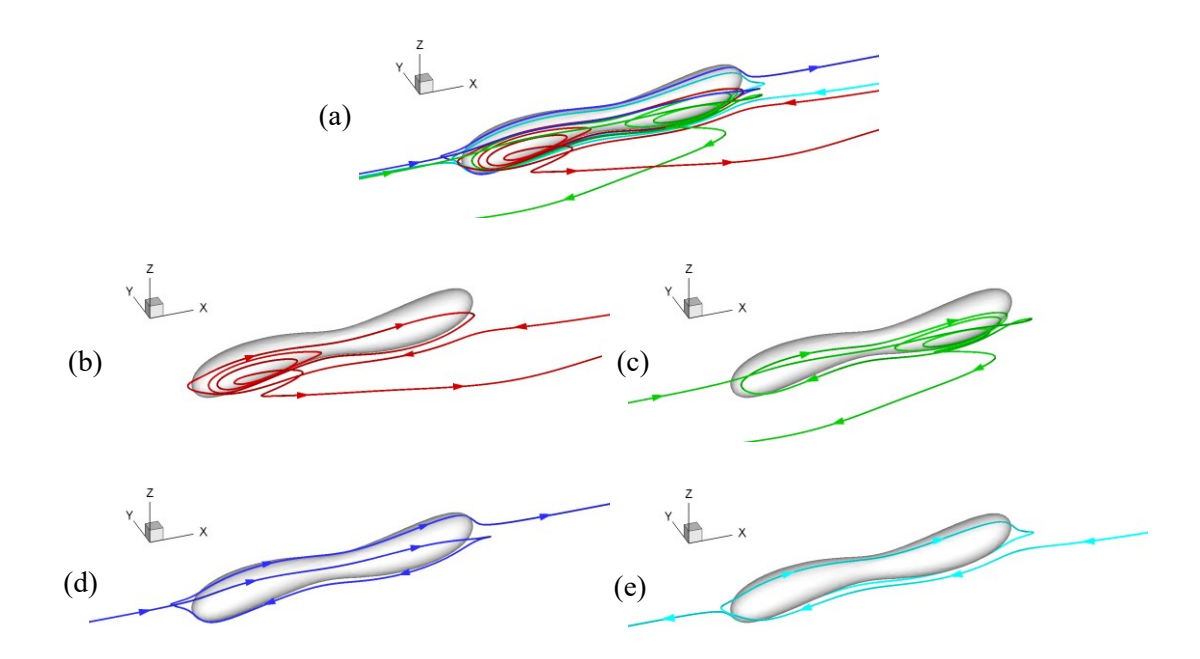


Fig. 16. Typical 3D streamlines around a droplet for Ca = 0.5 and Re = 0.01. (a) Overall pattern of streamlines around the droplet, (b, c) inward (decreasing radial coordinate), (d, e) outward (increasing radial coordinate) spiral flows on the sides.

An increase in Reynolds number can enhance droplet breakup. At larger Reynolds number, droplet breakup produces more and smaller child droplets. Figure 17 shows the process of a single droplet breaking up into many child droplets, as well as the process of scalar transport from the droplets, for Ca = 0.5, Re = 1, and Sc = 100. Due to the increased fluid inertia, the droplet is much elongated before it breaks up, compared to the case of Re = 0.01. Although the droplet breaks up into more child droplets, the basic process and mechanism of scalar transport are similar to those for Re = 0.01, shown in Figs. 15 and 16. The corresponding variation of Sh versus  $t/\tau_s$  is shown in Figure 18. The curve follows a similar trend as that for Re = 0.01, although Stage IV is not shown in the figure. In Stage I ( $t/\tau_s \leq 35$ ), the droplet elongation makes Sh increase linearly with time. In Stage II ( $35 \leq t/\tau_s \leq 50$ ), droplet breakup happens and Sh remains roughly constant. After that, the variation of Sh enters Stage III ( $50 \leq t/\tau_s \leq \Gamma$ , where  $\Gamma$  is the value separating Stages III and IV), where the distances between neighboring droplets increase and their influence on each other's scalar release is reduced. Because it will take a very long time for the child droplets to separate completely, Stage IV is not included in the figure. Figures 17 and 18 together reveal the variation in scalar release rate over the whole process of droplet breakup.

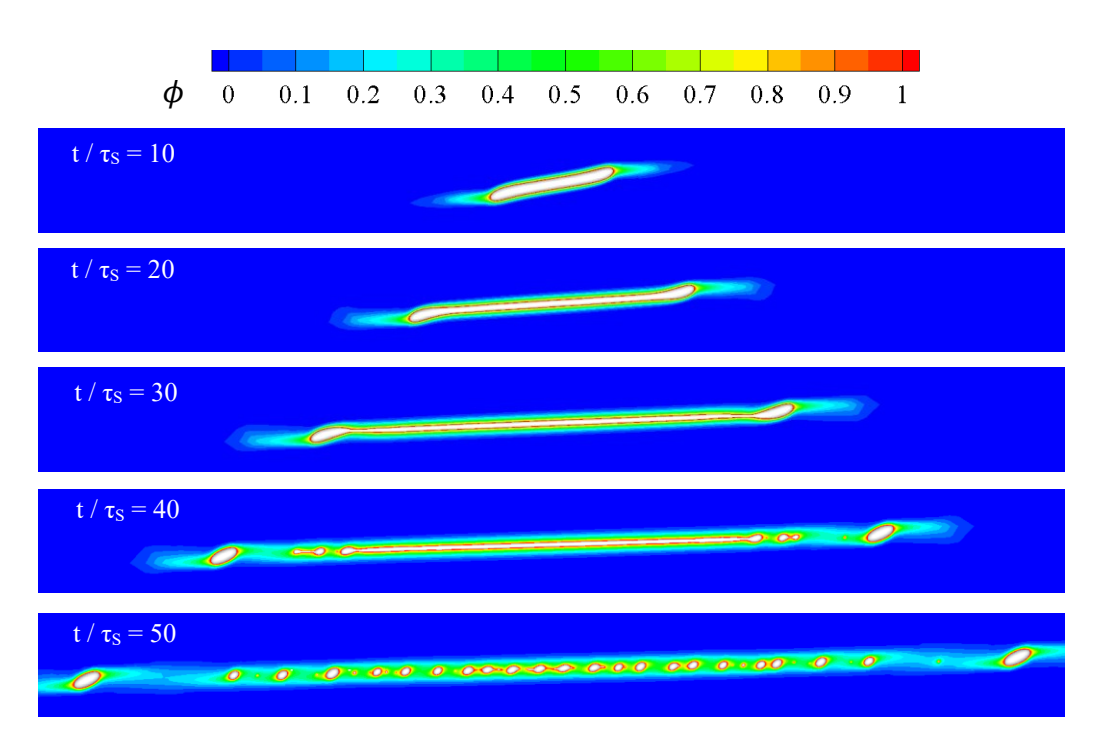


Fig. 17. Patterns of 3D droplet breakup for Ca = 0.5 and Re = 1 and scalar concentration on the central x-z plane for Sc = 100.

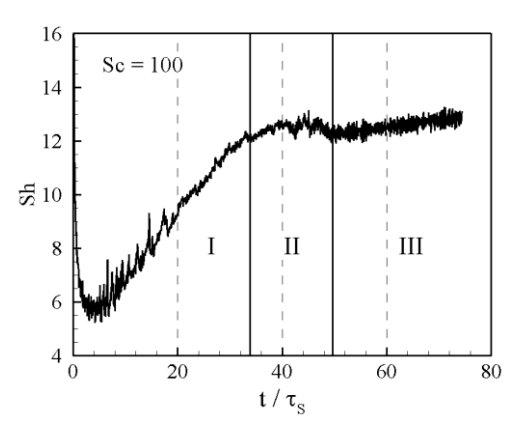


Fig. 18. Nondimensional scalar release rate from droplet: Sherwood number Sh versus time  $t/\tau_S$  for Ca = 0.5 and Re = 1.

Below, the case of droplet breakup will be discussed together with the nonbreakup case to give an overall picture. Figure 19 shows a regime diagram for droplet deformation and breakup in the space of Ca and Re, based on the results of the present numerical simulation. Note that this diagram only applies when the density and viscosity of the droplet are the same as those of the carrier fluid. As shown in the figure, both Ca and Re can enhance the droplet deformation and breakup. For a given Re, an increase in Ca leads to larger deformation when Ca is below a critical value  $Ca_{crit}$  where the droplet begins to break up, and an increase in Ca leads to finer breakup when  $Ca > Ca_{crit}$ . For a given Ca, increasing Re has the same effect.  $Ca_{crit}$  is dependent on

*Re*, and it decreases with an increase in *Re*. This is consistent with the observations in Renardy & Cristini<sup>31</sup>, Wagner et al.<sup>32</sup>, and Farokhirad et al.<sup>34</sup>.

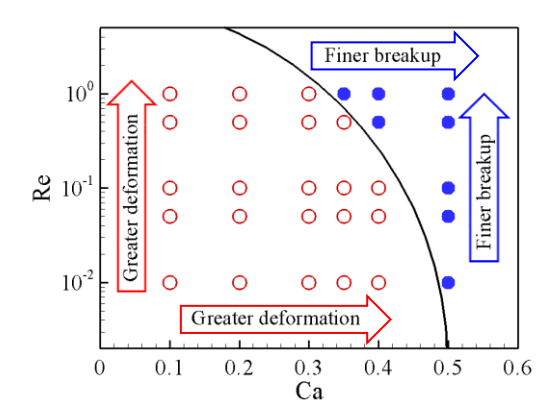


Fig. 19. Regime diagram of droplet deformation and breakup.

In Fig. 20 we compare the time variation of the amount of passive scalar released from the droplet  $M/V_d$  for Sc = 100, where  $V_d$  is the volume of the droplet and M is the amount of passive scalar, defined as  $M = \int \phi dV$ . The integration is only done in the carrier fluid. Time is normalized with both the characteristic diffusive time  $\tau_D$  and the flow shear time  $\tau_S$ .  $\tau_D$  is defined as  $R^2/D_m$ . Using  $t/\tau_D$  means that the diffusivity of passive scalar in the fluid is fixed, and the increase in Re represents the increase of flow shear rate. On the other hand, using  $t/\tau_S$  means that the flow shear rate is fixed, and the increase in Re represents the decrease in diffusivity for a given Schmidt number. The purpose of using  $t/\tau_D$  is to compare the scalar release under shear with that of pure diffusion. When Ca = 0.1 and 0.3, the droplet is elongated gradually to a stable shape, but when Ca = 0.5, the droplet breaks up into two or more child droplets. The slopes of the curves in the figure represent the scalar release rate. Compared with pure diffusion, the flow shear significantly enhances the release of passive scalar, and the enhancement is greater for larger Re, as shown in Fig. 20(a). In this study, the Sherwood number is defined as the ratio of scalar release rate under shear condition to that of pure diffusion (Eqn. (6)), so the curve slopes in Fig 20(a) are consistent with the Sherwood number shown in Fig. 12 and 13. When using  $t/\tau_S$ , passive scalar is released faster at smaller Reynolds numbers, due to the enhanced diffusion effect, as shown in Fig. 20(b). For the same Re, the case with a larger Ca always has a higher scalar release

rate, because of larger deformation or finer breakup. Figure 20 also shows that droplet breakup at Ca = 0.5 causes a significant increase in scalar release rate as compared to unbroken deformation at Ca = 0.1 and 0.3.

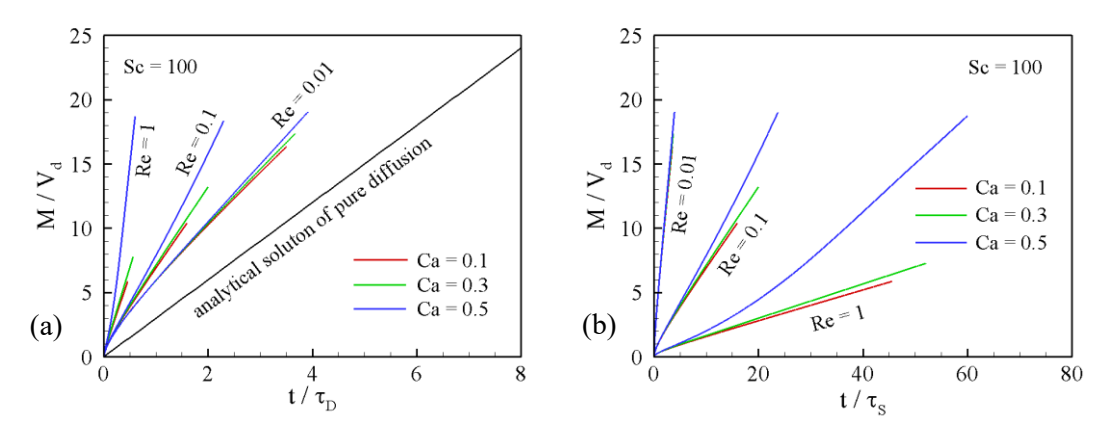


Fig. 20. Amount of passive scalar released from droplet versus time for typical capillary and Reynolds numbers. Sc = 100. (a) Time is normalized by diffusion time scale,  $\tau_D$ , (b) time is normalized by flow shear time scale,  $\tau_S$ .

Figure 21 shows Sherwood number versus Reynolds and capillary numbers for both unbroken and broken droplets. Two Schmidt numbers, Sc = 10 and 100 are included. For broken droplets, Sh is calculated when breakup is complete and Sh is close to a constant. For unbroken droplets, Ca does not influence the scalar release rate very much and Sh is mainly determined by Re and Sc. It has been shown in Fig. 13 that for unbroken droplets the dependence of Sh on Pe can be largely described by the model for a rigid sphere. For broken droplets, the problem becomes more complicated. Droplet breakup may be caused by an increase in Re or an increase in Ca. As soon as breakup happens, Sh increases sharply from that of the unbroken droplets, except in the cases with much stronger diffusion effect, such as Re = 0.01. For broken droplets, Sh changes much more sharply with Re and Ca than unbroken droplets. This implies that the increase is caused by the finer breakup with more child droplets, rather than enhanced advective transport. Although the variations of Sh demonstrate a similar trend on Re for different Ca, and also demonstrate a similar trend on Ca for different Re, the development of an empirical correlation of Sh will be more difficult than for unbroken droplets, because the effects of the number and size distribution of the child droplets after breakup must be considered.

Figure 22 shows Sherwood number versus Peclet number for both broken and unbroken droplets. As observed from Fig. 21, droplet breakup causes a sharp increase in *Sh*. This sharp change cannot be described

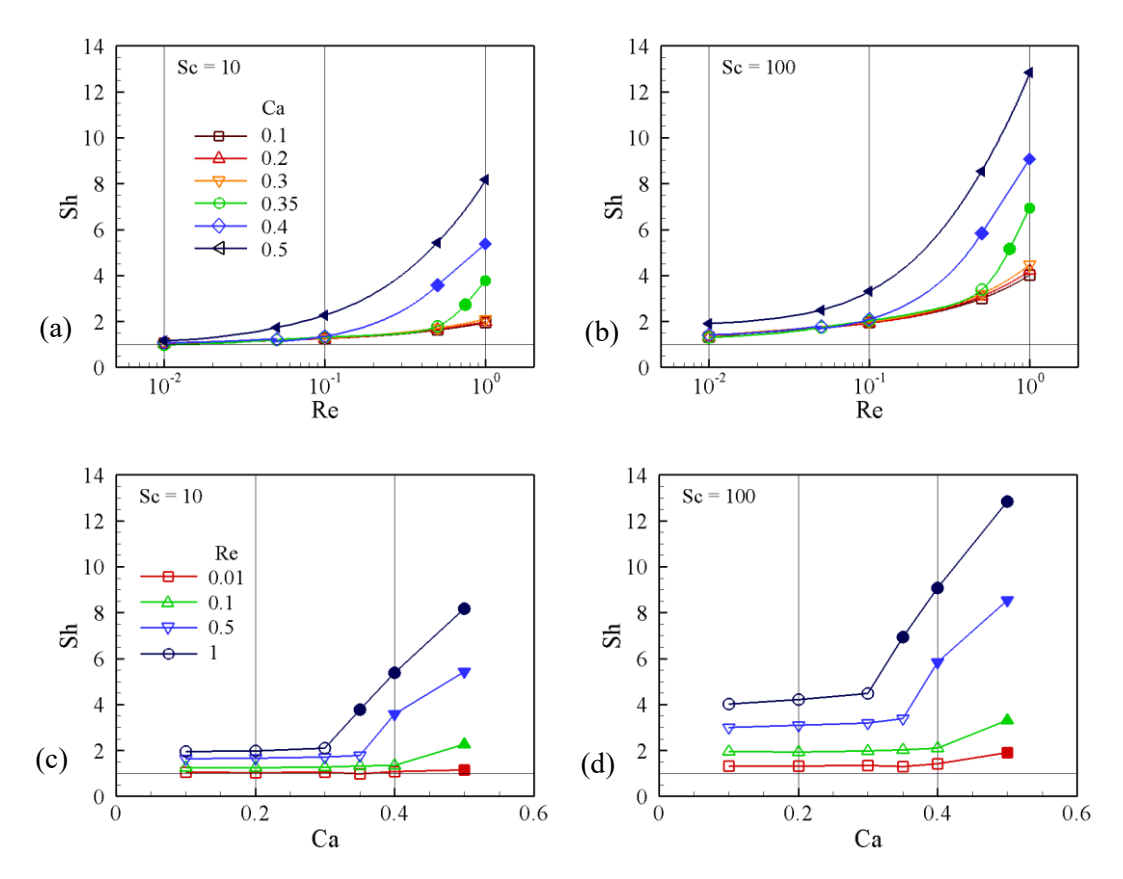


Fig. 21. Sherwood number versus Reynolds and capillary numbers. Hollow symbols represent unbroken droplets and solid symbols represent broken droplets. (a, b) Sh vs. Re, (c, d) Sh vs. Ca, (a, c) Sc = 10, (b, d) Sc = 100.

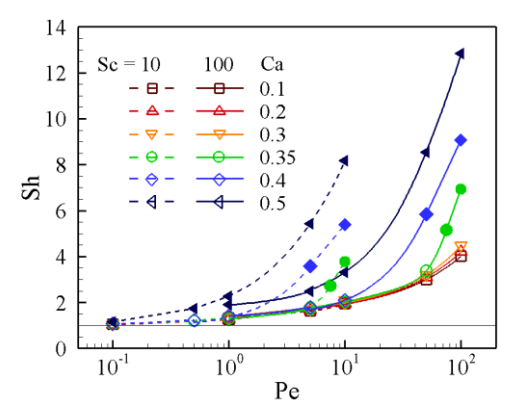


Fig. 22. Sherwood number versus Peclet number. Hollow symbols represent unbroken droplets and solid symbols represent broken droplets. (a) Unbroken droplets, (b) unbroken and broken droplets.

by models only involving *Re* and *Sc*. However, the curves exhibit a similar trend on *Pe*, which suggests that it will be feasible to develop an advanced model in the future, including the effect of droplet breakup characterized by capillary and Reynolds numbers.

## 6. Conclusion

Through high-fidelity numerical simulation based on a well-developed VOF-based CFD solver, we have conducted an in-depth study of the advection-enhanced heat and mass transport from a single droplet neutrally suspended in a simple shear flow. This paper focuses on addressing the following three issues, the complex flows caused by the interaction of suspended droplet and carrier fluid, the mechanism of advective enhancement of heat and mass transport induced by the complex flows around the droplet, and the effects of droplet deformation and breakup on heat and mass transport. In the simulation, the temperature and mass concentration are modeled as the concentration of a passive scalar released at droplet surface. The capillary number considered in this study ranges from 0.01 to 0.5, which encompasses the entire range of small deformation, large deformation, and breakup of the droplets. The Reynolds number is from 0.01 to 1, which includes regions of weak and strong advection. Two Schmidt numbers, 10 and 100, are considered, for which flow advection plays a role in the transport of passive scalar.

The evolution of the droplet morphology depends on the combination of capillary and Reynolds numbers. An increase in either capillary or Reynolds number can cause larger deformation of unbroken droplets and finer breakup. The critical capillary number at which the droplet breaks up decreases with the increase in Reynolds number.

For unbroken droplets, the interaction between the carrier fluid and suspended droplet leads to several flows around the droplet, which are characterized by streamlines of four types of patterns. These are: inward spiral flows on the lateral side, outward spiral flows near the equator, recirculating wake flows up- and downstream of the droplet near the flow axis, and outer passing flow wrapping the spiral and wake flows. The passive scalar released at the droplet surface is first transported through the fluid layer of the spiral flows to the outer passing flow via diffusion, and then transported downstream by the outer flow via advection. After leaving the droplet, the outer fluid passes a portion of the passive scalar to the fluid further outside and the fluid in the recirculating wake, which helps transport passive scalar downstream via advection. These flow motions, together with scalar diffusion, constitute a coupled transport mechanism for passive scalar from the

droplet to the far field. The droplet elongation caused by the increase in capillary number does not significantly increase the scalar release rate. The dependence of scalar release rate on Reynolds and Peclet numbers can be roughly described by the correlation for a rigid sphere.

For broken droplets, the basic features of the fluid flow around the droplet during the process of elongation and breakup are the same as those of an unbroken droplet in the stable state. There are both inward and outward spiral flows on the sides of each elliptical element of the droplet. Droplet breakup can significantly enhance the scalar release rate. The process of the variation of scalar release rate can be decomposed into several stages; the scalar release rate in each stage is related to the details of the droplet elongation and breakup processes. In the first stage, the scalar release rate increases roughly linearly with time, corresponding to the elongation of droplet in the flow direction. In the second stage, the release rate remains roughly constant, corresponding to the period of droplet breakup in which the extension of the droplet in the flow direction does not increase. In the third stage, the scalar release rate increases again, corresponding to the initial period of the separation of the child droplets, during which the child droplets influence each other's scalar release rate. In the last stage, the scalar release rate remains constant again, corresponding to the period in which the child droplets have completely separated and do not influence each other. The discovery that the release rate can be viewed in stages will facilitate the development of empirical models for the entire process of scalar release rate for broken droplets.

Compared with unbroken droplets, scalar release rates after the droplets complete breakup are significantly increased and far exceed the prediction range of traditional models for spherical droplets and rigid spheres. The variation of scalar release rate exhibits a high correlation with the capillary, Reynolds, and Peclet numbers. This suggests that it will in the future be feasible to develop an advanced empirical model, to incorporate the effects of the number and size distribution of child droplets after breakup.

#### **ACKNOWLEDGEMENTS:**

This work was supported by the National Science Foundation (Award ID: 2138740)

## **CONFLICT OF INTEREST:**

The authors have no conflicts of interest to disclose

## **DATA AVAILABILITY:**

The data that support the findings of this study are available from the corresponding author upon reasonable request.

## REFERENCES

- 1. L. Shui, J. C. Eijkel, and A. Van den Berg, "Multiphase flow in microfluidic systems—Control and applications of droplets and interfaces," Advances in colloid and interface science **133**, 35 (2007)
- 2. A. Huebner, S. Sharma, M. Srisa-Art, F. Hollfelder, J. B. Edel, and A. J. Demello, "Microdroplets: a sea of applications?," Lab on a Chip **8**, 1244 (2008).
- 3. H. Song, M. R. Bringer, J. D. Tice, C. J. Gerdts, and R. F. Ismagilov, "Experimental test of scaling of mixing by chaotic advection in droplets moving through microfluidic channels," Applied physics letters **83**, 4664 (2003).
- 4. E. M. Payne, D. A. Holland-Moritz, S. Sun, and R. T. Kennedy, "High-throughput screening by droplet microfluidics: Perspective into key challenges and future prospects," Lab on a Chip **20**, 2247 (2020).
- 5. B. Zheng, L. S. Roach, and R. F. Ismagilov, "Screening of protein crystallization conditions on a microfluidic chip using nanoliter-size droplets," Journal of the American chemical society **125**, 11170 (2003).
- 6. L. Li, and R. F. Ismagilov, "Protein crystallization using microfluidic technologies based on valves, droplets, and SlipChip," Annual review of biophysics **39**, 139 (2010).
- 7. S. L. Sjostrom, H. N. Joensson, and H. A. Svahn, "Multiplex analysis of enzyme kinetics and inhibition by droplet microfluidics using picoinjectors," Lab on a Chip 13, 1754 (2013).
- 8. D. Hess, T. Yang, and S. Stavrakis, "Droplet-based optofluidic systems for measuring enzyme kinetics," Analytical and bioanalytical chemistry **412**, 3265 (2020).
- 9. M. Delgado, A. Lázaro, J. Mazo, and B. Zalba, "Review on phase change material emulsions and microencapsulated phase change material slurries: Materials, heat transfer studies and applications," Renewable and Sustainable Energy Reviews 16, 253 (2012).

- 10. F. Goodarzi, and S. Zendehboudi, "A comprehensive review on emulsions and emulsion stability in chemical and energy industries," The Canadian Journal of Chemical Engineering 97, 281 (2019).
- 11. A. Kumar, A. Thakur, and P. S. Panesar, "A review on emulsion liquid membrane (ELM) for the treatment of various industrial effluent streams," Reviews in Environmental Science and Bio/Technology **18**, 153 (2019).
- 12. M. A. Hussein, A. A. Mohammed, and M. A. Atiya, "Application of emulsion and Pickering emulsion liquid membrane technique for wastewater treatment: an overview," Environmental Science and Pollution Research 26, 36184 (2019).
- 13. H. Hande Mert, and S. Şen, "Synthesis and characterization of polyHIPE composites containing halloysite nanotubes," e-Polymers **16**, 419 (2016).
- 14. Y. Fadil, S. C. Thickett, V. Agarwal, and P. B. Zetterlund, "Synthesis of graphene-based polymeric nanocomposites using emulsion techniques," Progress in Polymer Science 125, 101476 (2022).
- 15. T. Kuennen, "Polymers Add Performance to Asphalt Emulsions," Better Roads 74, (2004).
- 16. I. Boz, Y. S. Kumbargeri, and M. E. Kutay, "Performance-based percent embedment limits for chip seals," Transportation Research Record **2673**, 182 (2019).
- 17. F. Li, J. Shu, L. Zhang, N. Yang, J. Xie, X. Li, L. Cheng, S. Kuang, S.-Y. Tang, and S. Zhang, "Liquid metal droplet robot," Applied Materials Today 19, 100597 (2020).
- 18. A. Li, H. Li, Z. Li, Z. Zhao, K. Li, M. Li, and Y. Song, "Programmable droplet manipulation by a magnetic-actuated robot," Science advances 6, eaay5808 (2020).
- 19. Y. Zhu, L.-N. Zhu, R. Guo, H.-J. Cui, S. Ye, and Q. Fang, "Nanoliter-scale protein crystallization and screening with a microfluidic droplet robot," Scientific reports 4, 1 (2014).
- 20. Y. Wei, Y. Zhu, and Q. Fang, "Nanoliter quantitative high-throughput screening with large-scale tunable gradients based on a microfluidic droplet robot under unilateral dispersion mode," Analytical chemistry **91**, 4995 (2019).
- 21. M. Sattari-Najafabadi, M. N. Esfahany, Z. Wu, and B. Sunden, "Mass transfer between phases in microchannels: A review," Chemical Engineering and Processing-Process Intensification 127, 213 (2018).
- 22. I. Pioro, W. Rohsenow, and S. Doerffer, "Nucleate pool-boiling heat transfer. I: review of parametric effects of boiling surface," International Journal of Heat and Mass Transfer 47, 5033 (2004).
- 23. J. Lu, and G. Tryggvason, "Effect of bubble deformability in turbulent bubbly upflow in a vertical channel," Physics of Fluids **20**, 040701 (2008).
- 24. G. Tryggvason, and J. Lu, "Direct numerical simulations of flows with phase change," Procedia IUTAM 15, 2 (2015).
- 25. M. Dadhich, O. S. Prajapati, and V. Sharma, "A systematic review on the heat transfer investigation of the flow boiling process," Chemical Engineering and Processing-Process Intensification **165**, 108425 (2021).
- 26. X. Fan, X. Dong, A. C. Karacakol, H. Xie, and M. Sitti, "Reconfigurable multifunctional ferrofluid droplet robots," Proceedings of the National Academy of Sciences 117, 27916 (2020).
- 27. Y. Wang, B. Abrahamsson, L. Lindfors, and J. G. Brasseur, "Analysis of Diffusion-Controlled Dissolution from Polydisperse Collections of Drug Particles with an Assessed Mathematical Model," Journal of Pharmaceutical Sciences **104**, 2998 (2015).
- 28. G. I. Taylor, "The viscosity of a fluid containing small drops of another fluid," Proceedings of the Royal Society of London. Series A, Containing papers of a mathematical and physical character **138**, 41 (1932).
- 29. G. I. Taylor, "The formation of emulsions in definable fields of flow," Proceedings of the Royal Society of London. Series A, Containing papers of a mathematical and physical character **146**, 501 (1934).

- 30. H.P. Grace, "Dispersion phenomena in high viscosity immiscible fluid systems and application of static mixers as dispersion devices in such systems," Chemical Engineering Communications 14, 225 (1982).
- 31. Y. Y. Renardy, and V. Cristini, "Effect of inertia on drop breakup under shear," Physics of Fluids 13, 7 (2001).
- 32. A. Wagner, L. Wilson, and M. Cates, "Role of inertia in two-dimensional deformation and breakdown of a droplet," Physical review E **68**, 045301 (2003).
- 33. Y. Renardy, "The effects of confinement and inertia on the production of droplets," Rheologica acta **46**, 521 (2007).
- 34. S. Farokhirad, T. Lee, and J. F. Morris, "Effects of inertia and viscosity on single droplet deformation in confined shear flow," Communications in Computational Physics 13, 706 (2013).
- 35. M. Shapira, and S. Haber, "Low Reynolds number motion of a droplet in shear flow including wall effects," International journal of multiphase flow **16**, 305 (1990).
- 36. V. Sibillo, G. Pasquariello, M. Simeone, V. Cristini, and S. Guido, "Drop deformation in microconfined shear flow," Physical review letters **97**, 054502 (2006).
- 37. A. Vananroye, P. Van Puyvelde, and P. Moldenaers, "Effect of confinement on droplet breakup in sheared emulsions," Langmuir **22**, 3972 (2006).
- 38. H. Hua, Y. Li, J. Shin, H.-K. Song, and J. Kim, "Effect of confinement on droplet deformation in shear flow," International Journal of Computational Fluid Dynamics **27**, 317 (2013).
- 39. N. Ioannou, H. Liu, and Y. Zhang, "Droplet dynamics in confinement," Journal of Computational Science 17, 463 (2016).
- 40. A. Amani, N. Balcázar, J. Castro, and A. Oliva, "Numerical study of droplet deformation in shear flow using a conservative level-set method," Chemical Engineering Science **207**, 153 (2019).
- 41. S. Popinet, "Gerris: a tree-based adaptive solver for the incompressible Euler equations in complex geometries," Journal of Computational Physics **190**, 572 (2003).
- 42. S. Popinet, "An accurate adaptive solver for surface-tension-driven interfacial flows," Journal of Computational Physics 228, 5838 (2009).
- 43. Y. Wang, and J. G. Brasseur, "Enhancement of mass transfer from particles by local shear-rate and correlations with application to drug dissolution," AIChE Journal 65, e16617 (2019).
- 44. Y. Wang, H. Wan, R. Gonzalez Pizarro, S. Lim, and F. Shu, "Heat and mass transport from neutrally suspended oblate spheroid in simple shear flow," Physics of Fluids **35**, 033319 (2023)
- 45. R. K. Singh, and K. Sarkar, "Inertial effects on the dynamics, streamline topology and interfacial stresses due to a drop in shear," Journal of fluid mechanics **683**, 149 (2011).
- 46. P. Maffettone, and M. Minale, "Equation of change for ellipsoidal drops in viscous flow," Journal of Non-Newtonian Fluid Mechanics **78**, 227 (1998).
- 47. A. Vananroye, P. Van Puyvelde, P. Moldenaers, "Effect of confinement on the steady-state behavior of single droplets during shear flow," Journal of Rheology **51**, 139 (2007).
- 48. S. Guido, and M. Villone, "Three-dimensional shape of a drop under simple shear flow," Journal of Rheology **42**, 395 (1998).
- 49. S. Guido, F.Greco, and M. Villone, "Experimental determination of drop shape in slow steady shear flow," Journal of Colloid and Interface Science **219**, 298 (1999).
- 50, S. Guido, and F. Greco, "Drop shape under slow steady shear flow and during relaxation. Experimental results and comparison with theory. Rheologica acta, **40**, 176 (2001).

- 51. J. Gounley, G. Boedec, M. Jaeger, and M. Leonetti, "Influence of surface viscosity on droplets in shear flow. Journal of Fluid Mechanics, **791**, 464 (2016).
- 52. N. A. Frankel, and A. Acrivos, "Heat and mass transfer from small spheres and cylinders freely suspended in shear flow," The Physics of Fluids 11, 1913 (1968).
- 53. A. Acrivos, "Heat transfer at high Peclet number from a small sphere freely rotating in a simple shear field," Journal of fluid mechanics **46**, 233 (1971).
- 54. G. Batchelor, "Mass transfer from a particle suspended in fluid with a steady linear ambient velocity distribution," Journal of fluid mechanics **95**, 369 (1979).
- 55. A. Polyanin, and V. Dil'man, "New methods of the mass and heat transfer theory—II. The methods of asymptotic interpolation and extrapolation," International Journal of Heat and Mass Transfer 28, 45 (1985).